Available online at www.sciencedirect.com
ScienceDirect
Trans. Nonferrous Met. Soc. China 35(2025) 486−498

Transactions of Nonferrous Metals Society of China
www.tnmsc.cn

Hot deformation characteristics and dynamic recrystallization of Ti−6Al−4V−0.5Mo−0.5Zr alloy used for petroleum drill pipe

Zhen-ni ZHOU[1], Gao-yong LIN[1], Yu-hao AI[1], Wei-zhong FENG[2], Ping-hui ZHANG[2], Hui-qun LIU[1]

1. School of Materials Science and Engineering, Central South University, Changsha 410083, China;
2. Baoji Titanium Industry Co., Ltd., Baoji 721014, China

Received 14 August 2023; accepted 26 March 2024

Abstract: The high-temperature compression deformation behavior of Ti−6Al−4V−0.5Mo−0.5Zr alloy was investigated at temperatures from 890 to 1030 °C and strain rates from 0.01 to 10 s^{-1}, and the corresponding dynamic recrystallization (DRX) mechanism was revealed. The results indicate that under different deformation conditions, the intensity of flow stress oscillations varied significantly. During thermal deformation in the $\alpha+\beta$ phase region, the stress−strain curves exhibited DRX. At temperatures below 950 °C, continuous dynamic recrystallization (CDRX) of the α grains and fracturing of the strip-like phase were apparent. At temperature higher than 950 °C, the β phase and a part of secondary α colonies underwent DRX.

Key words: titanium alloy; stress–strain curves; stress oscillation; dynamic recrystallization

---

1 Introduction

Titanium alloys have extensive applications in various fields including biomedicine, aerospace, automotive, shipbuilding, and oil exploration, owing to their excellent comprehensive properties [1−4]. Ti−6Al−4V−0.5Mo−0.5Zr alloy is a newly developed high-performance titanium alloy designed for petroleum drilling pipe in harsh environments. One of the routes for production of drilling pipe includes forging and extrusion, the alloy blank would experience high temperature flow process which affects microstructure and properties of extruded pipe. However, high temperature deformation ability of titanium alloys is limited in some degree due to low thermal conductivity and relative narrow hot working window [5,6].

In general, the mechanical characteristics of alloy are substantially influenced by the evolution of microstructure, which plays a pivotal role of deciding the work hardening (WH) and softening phenomena during high temperature deformation. To achieve optimal mechanical properties, it is necessary to control the dynamic softening such as dynamic recrystallization (DRX), dynamic recovery (DRV), and superplasticity during high temperature deformation [7−9]. Previous studies have shown that the high-temperature deformation behaviors of $\alpha+\beta$ titanium alloys are complex and highly dependent on deformation parameters [10−12]. In recent years, some studies have focused on the hot deformation behavior and microstructure evolution of high-performance titanium alloys under high temperature compression conditions [13]. The transition of β phase (stable at high temperatures) into α phase (stable at lower temperatures) is significantly influenced by the chemical composition of alloy and its mechanical processing conditions [14−16]. HUANG et al [17] investigated

---

Corresponding author: Hui-qun LIU, Tel: +86-13975809193, E-mail: liuhuiqun@csu.edu.cn
DOI: https://doi.org/10.1016/S1003-6326(24)66694-X

the microstructure evolution during the hot deformation of a high-strength titanium alloy. They primarily examined $\alpha \rightarrow \beta$ transformation and the precipitation of α phase in $\alpha+\beta$ phase region during high-temperature deformation. GANGIREDDY [18] researched Ti−6Al−4V with three different initial microstructures under varying cooling rates. The study revealed that the samples exhibited analogous high temperature softening characteristics. Therefore, investigating the hot deformation behavior of Ti−6Al−4V−0.5Mo−0.5Zr alloy under a specific initial condition is a key to exploring the thermal deformation patterns of this alloy.

During one of the production processes, hot-forged round billet of Ti−6Al−4V−0.5Mo−0.5Zr alloy was hot-extruded into pipe, therefore, in order to provide guidance for optimizing extrusion conditions, one of important factors is to acquire insights into the flow behavior and microstructural evolution mechanism during high temperature deformation. Here, we conducted isothermal compression tests on hot-forged Ti−6Al−4V−0.5Mo−0.5Zr alloy under various deformation conditions to obtain true stress−strain behavior, α phase fragment and DRX mechanism.

2 Experimental

The material used in this study was hot-forged round billets of Ti−6Al−4V−0.5Mo−0.5Zr alloy. The chemical composition of the alloy is listed in Table 1. Cylindrical specimens of 10 mm in diameter and 12 mm in height were prepared from the hot-forged billets for use in isothermal compression tests. Figure 1 shows electron backscatter diffraction (EBSD) maps of the hot-forged specimens. In Fig. 1(a), a bimodal microstructure can be identified in the image quality (IQ) map. Figure 1(b) shows the inverse pole figure (IPF) map of the alloy, where the low-angle grain boundaries (LAGBs, 2°−15°) and high-angle grain boundaries (HAGBs, >15°) are represented by pink and blue lines, respectively. The equiaxed α phase had an average grain size of 15.58 μm and a volume fraction of 38.72%. The secondary elongated α phase had a thickness of 6.71 μm and a volume fraction of 58.91%. Figure 1(c) reveals a small amount of the intergranular reticular β phase in the detection area, accounting for a volume fraction of 2.44%. The $\alpha \rightarrow \beta$ transus temperature was determined to be 963 °C, using metallographic method.

The isothermal compression tests were conducted using a thermal/mechanical machine (Gleeble 3500, Dynamic Systems Inc.) along the axial direction parallel to the hot-compression direction. Additionally, to reduce the friction between the specimens and the mold head, a 0.2 mm-deep pit was machined on both ends of each specimen, filled with high-temperature lubricant, and then covered with tantalum sheets. The cylindrical specimens

Table 1 Chemical composition of Ti−6Al−4V−0.5Mo−0.5Zr alloy (wt.%)

Al	V	Mo	Zr	Ca	Fe	Si	Ti
6.1504	4.0215	0.6527	0.7034	0.0039	0.0982	0.0055	Bal.

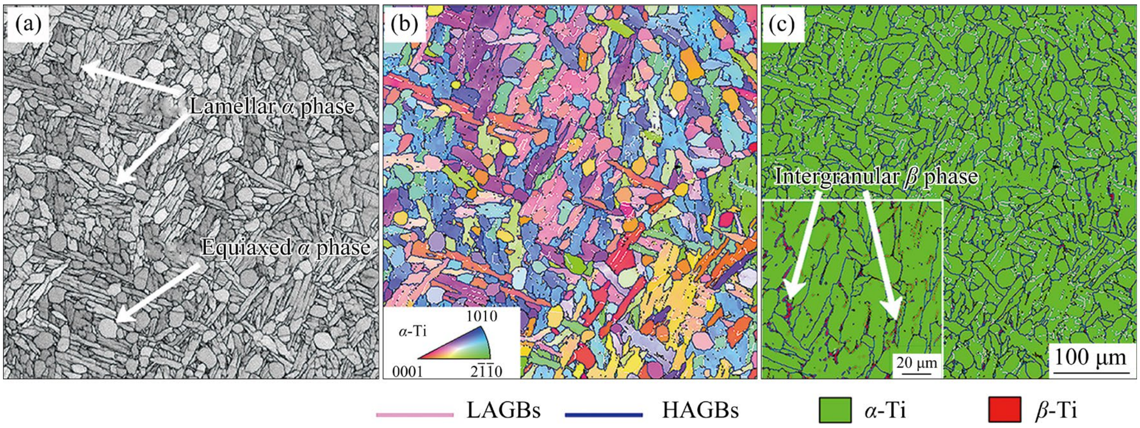

Fig. 1 EBSD maps showing initial microstructure of hot-forged Ti−6Al−4V−0.5Mo−0.5Zr alloy: (a) Image quality (IQ) map; (b) Inverse pole figure (IPF); (c) Phase distribution map

were heated to the deformation temperature at a rate of 5 °C/s and maintained at the setting temperature for 5 min to ensure that they were heated uniformly. Isothermal compression test was performed at temperatures of 890−1030 °C and strain rates of 0.01−10 s^{-1}. The maximum height reduction among the specimens during the compression tests was 60%. After deformation, the specimens were cooled in air to prevent cracking.

Following the thermal compression experiments, microstructure was observed for a cross section parallel to the compression axis. The samples were polished with emery paper and mechanically polished with OPS (silicon suspension) mixed with 15% hydrogen peroxide. The polished samples with smooth surfaces were observed by electron channeling contrast imaging (ECCI) using a field-emission scanning electron microscope (FE-SEM; TescanMira4) equipped with the NordlysMax3 collection system. The metallographic etching solution was prepared at a HNO_3:HF:H_2O volume ratio of 1:1:8, with an etching time of 3−5 s. Metallographic images were obtained using an optical microscope (OM, OLYMPUS). The samples for EBSD measurements were electropolished using a solution containing CH_3OH and $HClO_4$ at a volume ratio of 19:1. The power supply voltage was 30 V, and the polishing was conducted at room temperature during 30 s. The EBSD data were collected using a FE-SEM (TescanMira4) equipped with an EBSD analysis system, with an average scanning area of 140 μm × 140 μm and a step size of 0.4 μm. The EBSD data were analyzed using the OIM analysis software.

3 Results and discussion

3.1 Stress–strain curves

The data from the Gleeble tests conducted under different deformation conditions were corrected using friction effects and temperature elimination. The corrected true stress–strain curves for Ti−6Al−4V−0.5Mo−0.5Zr alloy under different conditions are shown in Fig. 2.

At a constant strain rate, the flow stress decreased with increasing deformation temperature.

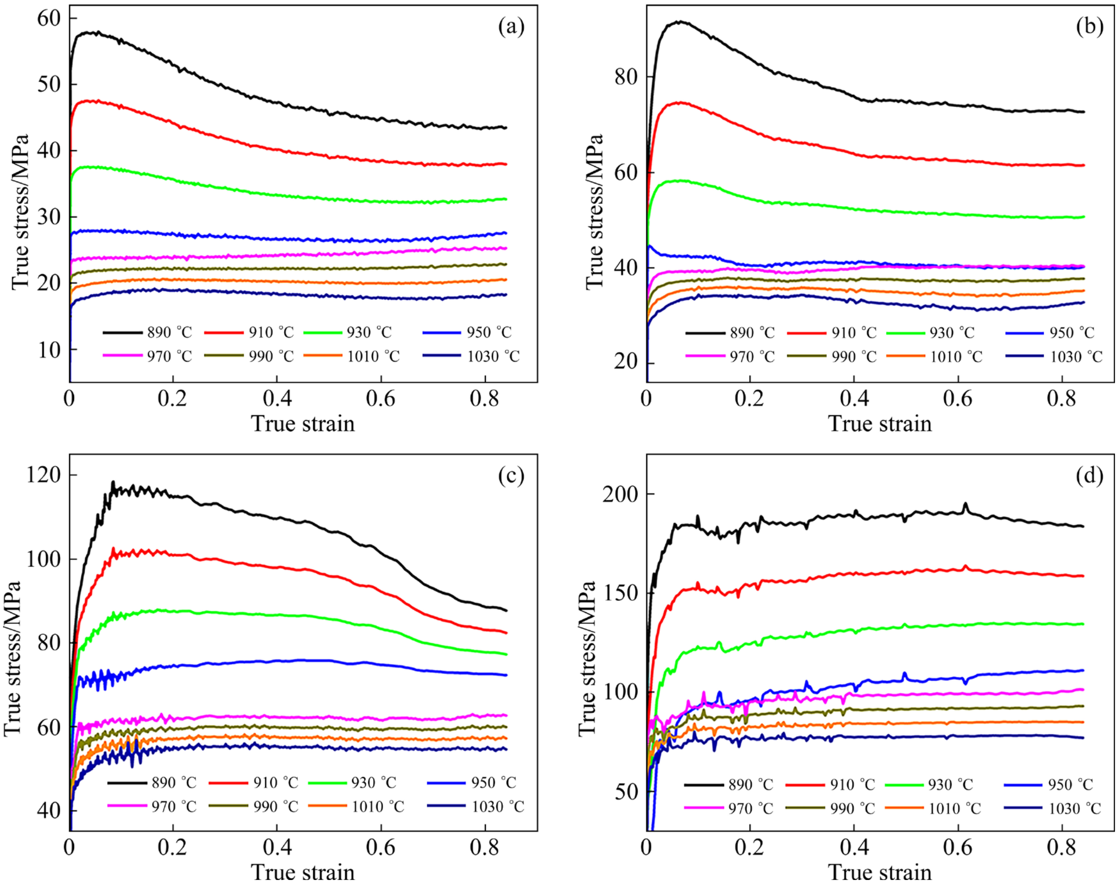

Fig. 2 Stress−strain curves of Ti−6Al−4V−0.5Mo−0.5Zr alloy under different deformation conditions: (a) $\dot{\varepsilon}$=0.01 s^{-1}; (b) $\dot{\varepsilon}$=0.1 s^{-1}; (c) $\dot{\varepsilon}$=1 s^{-1}; (d) $\dot{\varepsilon}$=10 s^{-1}

Higher temperature provided more energy for grain growth and promoted the formation of dislocation and subgrain boundary, hence, the promoted DRX phenomenon reduced flow stress. However, when the temperature approached $\alpha \rightarrow \beta$ transus temperature, an internal phase transition to β phase occurred [19]. Therefore, owing to the high plasticity of β phase, the resistance to deformation of alloy decreased, which reduced the stress required for deformation. Moreover, titanium alloys have low thermal conductivity. Hence, when both temperature and strain rate are increased, the heat generated by deformation caused a localized temperature increase if it is not readily dissipated, which further reduces the flow stress [20,21].

At a constant deformation temperature, the flow stress increased with increasing strain rate. This can be explained by dislocation kinetics [22,23]. The equation is expressed as follows:

$$\dot{\varepsilon} = \rho b v \tag{1}$$

where $\dot{\varepsilon}$ is the strain rate, ρ is the dislocation density, b is the amplitude of Burgers vector of perfect dislocations, and v is the average dislocation velocity.

The velocity of dislocation movement increased with increasing strain rate. Nonetheless, owing to the presence of lattice friction and the influence of solute atom, the velocity of dislocation movement increased up to a certain threshold and then reached a stable state. Consequently, a further rise in the strain rate led to a sharp increase of dislocation density, and eventually an increase of the true stress. Moreover, the deformation resistance decreased with increasing temperature because of the increase of the average atomic kinetic energy and the sharp decrease of the critical slip shear stress.

Figure 2 reveals that the variations in the flow stress were caused by the competing working hardening and dynamic softening mechanisms during hot deformation. In the early stage of deformation, the flow stress increased sharply as the degree of deformation increased. This is because strain accumulated in the alloy, causing dislocation to tangle and pile up. This increased the dislocation density, which resulted in working hardening. When the strain and accumulated deformation energy reached a critical point, dynamic softening started. Subsequently, as the curve stabilized, the working hardening and dynamic softening reached a dynamic equilibrium. As shown in Figs. 2(a–c), when the deformation temperature was less than 950 °C, the flow stress increased sharply with a slight increase in the strain (ε<0.02), reached a well-defined peak stress, and then decreased with increasing strain until it reached a steady state. In this case, the main softening mechanism was DRX, according to the characteristics of the flow curve. When the deformation temperature was higher than 950 °C, the flow stress increased sharply with a slight increase in the strain (ε<0.05). After peaking, the flow stress subsequently tended to stabilize as the strain increased. In this case, the main softening mechanism was DRV.

At higher strain rates ($\dot{\varepsilon}$=1−10 s^{-1}), cyclic or multi-peak flow stress occurred. This phenomenon was called discontinuous yielding. Discontinuous yielding has been observed in many previous studies at higher deformation temperature and strain rate [24,25]. It is considered to be a manifestation of the interaction between working hardening and DRV. As the strain rate increased, stress-oscillation phenomena were observed, in accordance with Figs. 2(c, d), which indicates that DRX occurred at a certain temperature and strain rate or in an unstable state [26].

The stress fluctuation at a strain rate of 1 s^{-1} was often related to dislocation plugging. The dislocation plugging at grain boundaries caused by large deformation led to stress concentration and broke up grain boundary, which rapidly crystallized and nucleated at high temperatures, releasing a large amount of energy and causing a local stress reduction. When the strain rate reached 10 s^{-1}, the flow instability was significant, and abrupt change occurred. This is because at high strain rate, a large amount of heat of deformation could not be readily conducted, resulting in localized high temperature and leading to inhomogeneous deformation. As illustrated in Fig. 3, unlike in the “belly” samples at lower strain rate, the waist crumpling phenomenon occurred when the strain rate reached 10 s^{-1}, which is attributable to the greater uneven deformation caused by the higher strain rate. This phenomenon is also observed in some other dual-phase titanium alloys and is unfavorable to the processing performance [27−29].

Fig. 3 Macroscopic morphology of Ti−6Al−4V−0.5Mo−0.5Zr alloy samples compressed at high temperatures

Flow stress curves are affected by a variety of deformation mechanisms. Therefore, it is difficult to determine the specific deformation mechanisms involved from the flow stress curves alone.

3.2 Microstructure analysis

3.2.1 Microstructure evolution during high temperature deformation

Some notable differences in microstructure were observed between the $\alpha+\beta$ and β phase regions after hot deformation. The radial direction (RD) is parallel to the CD. When the deformation temperature was 890−950 °C, a portion of the initial equiaxed α phase and the elongated strip-like α phase resulting from compression remained within the micro- structure, as illustrated in Figs. 4(a−f). Therefore, the $\alpha\rightarrow\beta$ transformation was incomplete, and the residual high-temperature α phase persisted. The residual α phase was located along the β phase grain boundary and became nucleation sites for a secondary α phase that formed during cooling. As the deformation temperature increased, the degree of transformation to β-phase increased and the proportion of the initial α grains gradually decreased. Figures 4(a−d) show that the proportion of initial grain (including deformed grain) decreased from 67.23% to 14.77% as the temperature rose from 890 to 950 °C. Furthermore, an increase in the strain rate resulted in a higher proportion of α grain that remained partially transformed, as depicted in Figs. 4(d−f). This can be attributed to the excessive strain rate at a specific temperature, which resulted in a relatively short transition period and an incomplete phase transformation. In $\alpha+\beta$ region, long strips of α grain fractured to form parts of fine approximate equiaxial α phase, as shown in Fig. 4(c).

A finer microstructure was observed at the deformation temperature ranged of 970−1030 °C, as depicted in Figs. 4(g−l). Therefore, a higher magnification was required to compare the microstructures in $\alpha+\beta$ and β phase regions. For this temperature range, the microstructure initially consisted of fine-sheet α phase. However, when the temperature exceeded the phase transition temperature, the alloy underwent a complete $\alpha\rightarrow\beta$ transition, and the β phase became dominant during deformation. Upon cooling, a significant number of elongated α phase lamellar precipitated from the β phase grain boundary, which contributed to the structure of the β transformation along with the remaining β phase [30].

Figure 4(k) shows fine equiaxed primary β grain, which suggests that DRX was the deformation mechanism under these conditions. Conversely, Fig. 4(j) shows larger equiaxed β grains. This can be attributed to higher temperature and lower strain rate, which provided additional energy and sufficient time for grain growth. The emergence of elongated serrated grain boundary, shown in Figs. 4(g−h), can be ascribed to the DRX of β grain, the subsequent growth of the recrystallized grains, and the nucleation of grain boundaries in an arch-like manner. In general, DRX improves the fluidity and thermal workability of a metal by causing softening and the formation of fine equiaxed grains during thermal deformation. The α phase in titanium alloys with hcp crystal structures exhibits limited plasticity. While, the β phase with body-centered cubic crystal structures has good plasticity. During hot working at elevated temperature, an increased β phase content results in a reduction in deformation resistance. This is beneficial for the hot working of Ti−6Al−4V−0.5Mo−0.5Zr. In summary, DRV and DRX occur in the $\alpha+\beta$ phase region during thermal deformation. These processes enhance the dynamic softening compared to the deformation in β phase region. In β phase region, DRV is the primary thermal deformation mechanism, yielding a thermal activation energy similar to that found in other titanium alloys [31,32].

3.2.2 Fragment of lamellar α

As depicted in Fig. 5, at the deformation temperature of 910 °C, small α phase sphere or block-like grain formed chain structure under the different strain conditions. This suggests that the strip-like α phase underwent bending and fracturing during deformation. With an increase in strain rate, the proportion of bent and twisted α phase strips

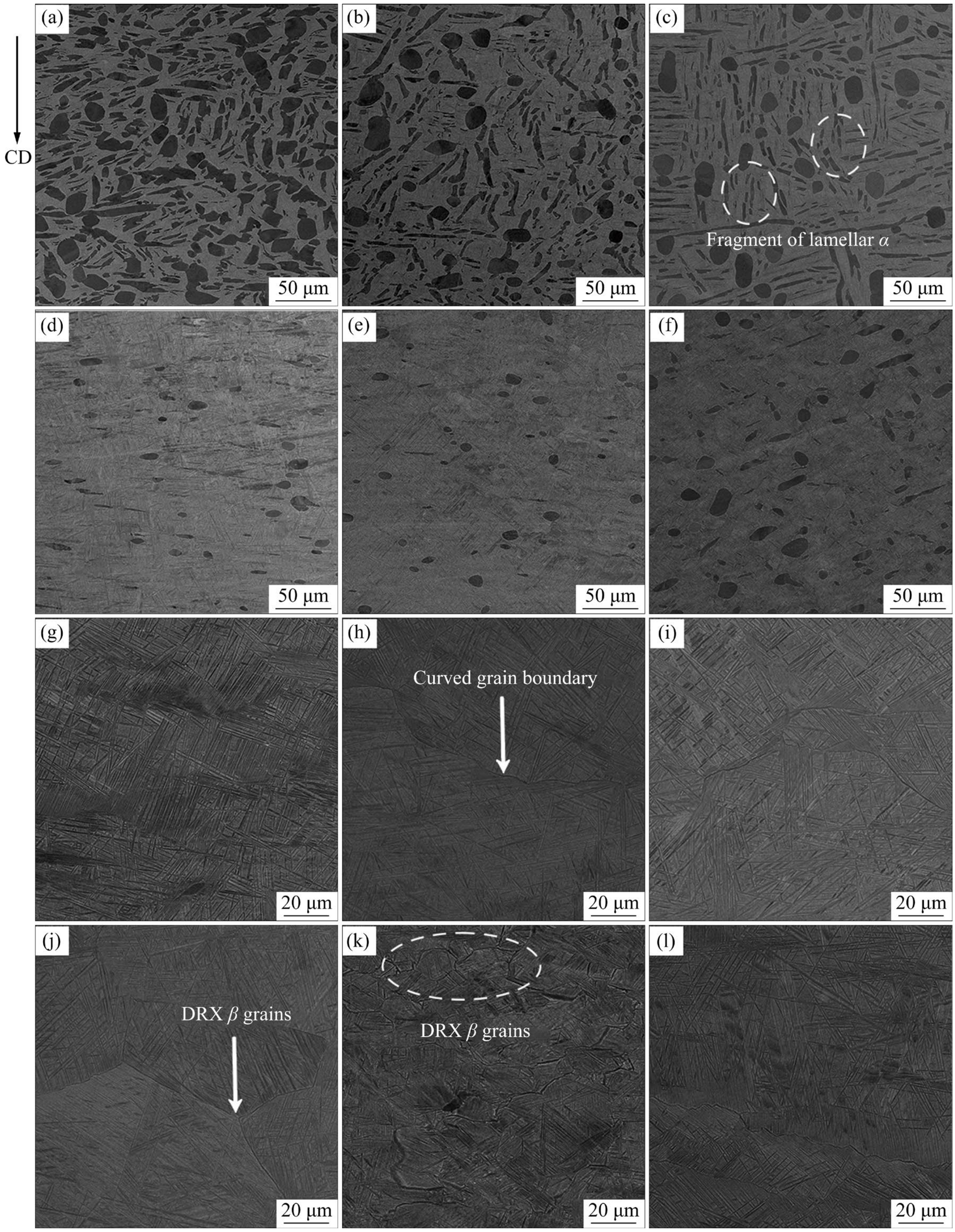

Fig.4 SEM images of Ti−6Al−4V−0.5Mo−0.5Zr alloy samples deformed under different deformation conditions: (a) T=890 °C, $\dot{\varepsilon}$=0.01 s^{-1}; (b) T=910 °C, $\dot{\varepsilon}$=0.01 s^{-1}; (c) T=930 °C, $\dot{\varepsilon}$=0.01 s^{-1}; (d) T=950 °C, $\dot{\varepsilon}$=0.01 s^{-1}; (e) T=950 °C, $\dot{\varepsilon}$=0.1 s^{-1}; (f) T=950 °C, $\dot{\varepsilon}$=10 s^{-1}; (g) T=970 °C, $\dot{\varepsilon}$=0.01 s^{-1}; (h) T=990 °C, $\dot{\varepsilon}$=0.01 s^{-1}; (i) T=1010 °C, $\dot{\varepsilon}$=0.01 s^{-1}; (j) T=1030 °C, $\dot{\varepsilon}$=0.01 s^{-1}; (k) T=990 °C, $\dot{\varepsilon}$=1 s^{-1}; (l) T=990 °C, $\dot{\varepsilon}$=10 s^{-1}

gradually decreased, whereas the proportion of fragmented fine α increased. In accordance with Figs. 5 and 6, the number of long α-phase strips decreased significantly with increasing strain rates. Measuring the length of grain in the observed area using the Image-Pro Plus software revealed that the average grain length decreased from 15.5679 to 8.3437 μm with an increase in the strain rate, which

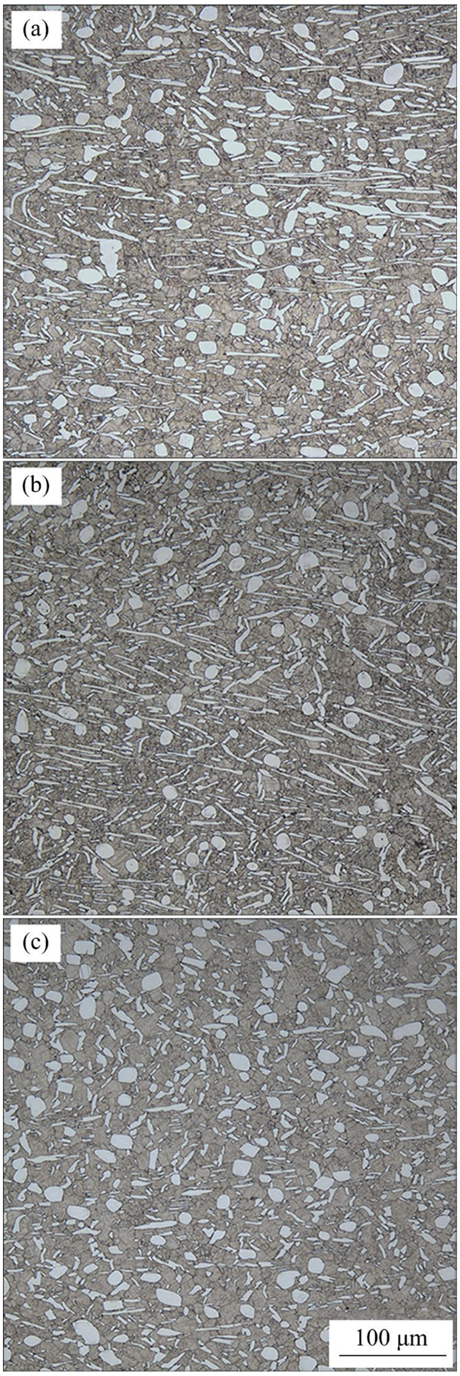

Fig. 5 Optical microstructure of Ti−6Al−4V−0.5Mo−0.5Zr alloy samples deformed at 910 °C and different strain rates: (a) $\dot{\varepsilon}$=0.01 s^{-1}; (b) $\dot{\varepsilon}$=1 s^{-1}; (c) $\dot{\varepsilon}$=10 s^{-1}

is because a large amount of laminated *α* phase underwent bending fracture after thermal deformation at high strain rates, forming an approximately equiaxial *α* phase. In the investigation of the thermal deformation of some dual-phase titanium alloys [33], numerous twisted strip grains were observed at 900 °C. Nevertheless, no distinct *α* strip phase fragment occurred. A previous study showed that the lamellar *α* phase is more likely to undergo bucking and kinking at high strain rates [17]. As illustrated in Fig. 5, the residual lamellar *α* phase is mostly perpendicular to the CD, and a buckle or even a fracture is more likely to occur when the striated grain is close to the CD.

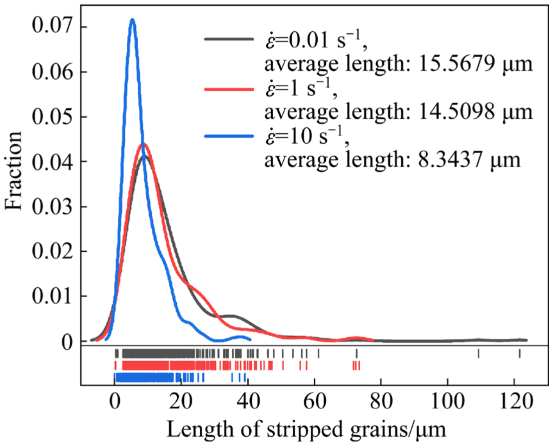

Fig. 6 Length distribution of stripped grain at 910 °C and different strain rates

WANG et al [34] proposed that softening behavior (such as DRX) originated from plastic deformation near grain boundary and the local accumulation of high strain energy caused by lamellar bending. Figure 7(b) shows lots of fine grains at the intersections of the grain boundary of the strip-like phase, which indicates that DRX started at grain boundary. Furthermore, as the strain rate increased, the strip-like phase became more twisted and fractured, as demonstrated in Fig. 5, which further increased the softening degree. The observations of the softening stages depicted in the stress−strain curve are shown in Fig. 2.

3.2.3 Dynamic recrystallization behavior

EBSD analysis was used to characterize the microstructure of the alloy deformed under different conditions for revealing recrystallization mechanism. The EBSD maps are represented in Fig. 7. Figures 7(b) and (e) show more refined grains containing HAGBs. Furthermore, there are more HAGBs than LAGBs, which suggests that most of fine grains appear through DRX. The fine DRX grains are concentrated at the edge of the large deformed grain, which indicates that DRX begins at the large deformed grains. Referring to Figs. 7(h) and (k), when the deformation temperature was higher than *α*/*β* transition temperature, the *α* phase with plate-like or clustered

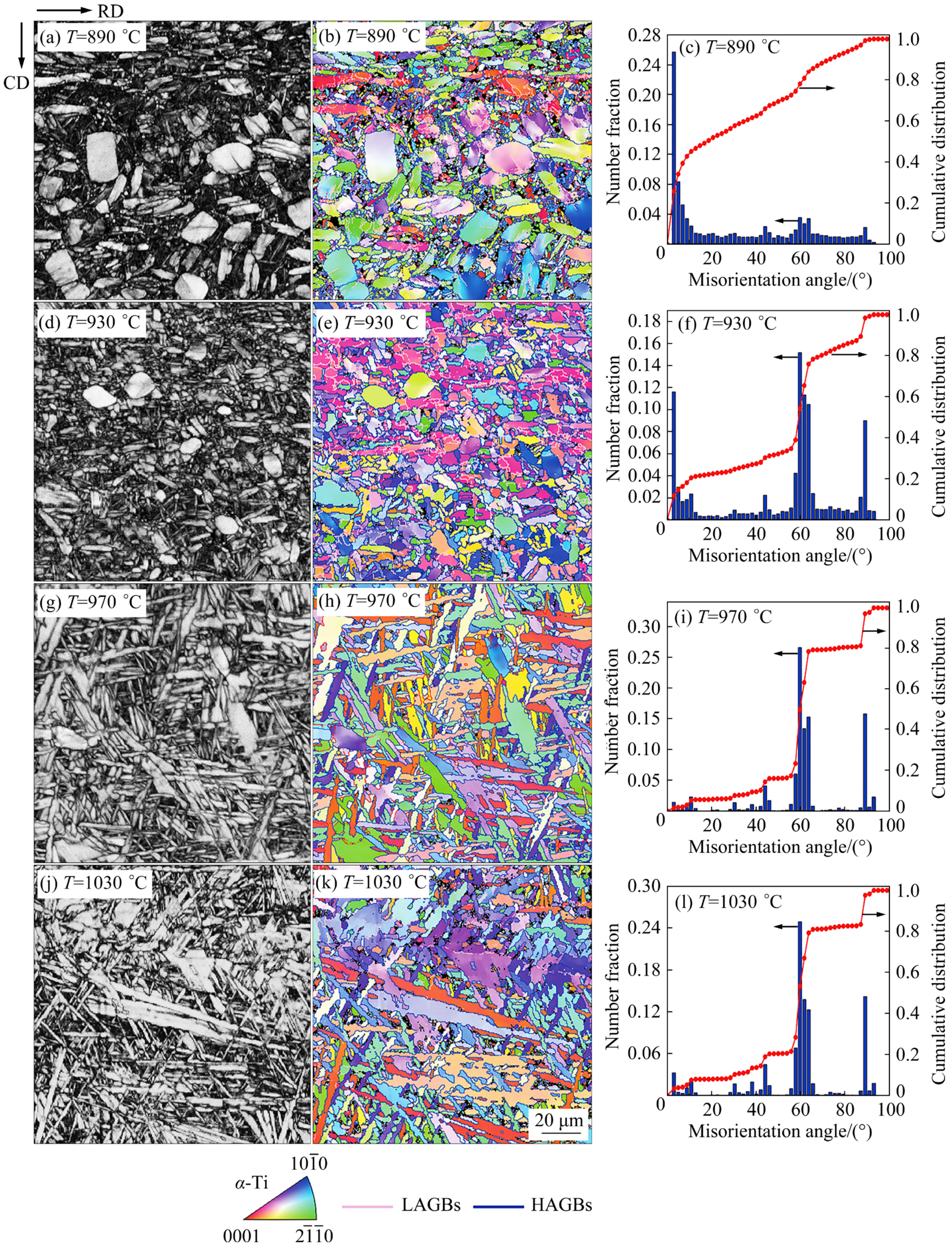

Fig. 7 EBSD microstructure analysis results of Ti−6Al−4V−0.5Mo−0.5Zr alloy samples at different temperatures and strain rate of 10 s^{-1}: (a, d, g, j) Microscopic morphology maps; (b, e, h, k) IPF maps; (c, f, i, l) Misorientation angle distribution charts

structure precipitated within β grain after cooling. In addition, there are some spherical and short rod-shaped fine grains. By combining these observations with the results depicted in Figs. 8(c, d), it can be deduced that these fine grains are recrystallized grains that formed via DRX of the previously precipitated intragranular plate-like α phase.

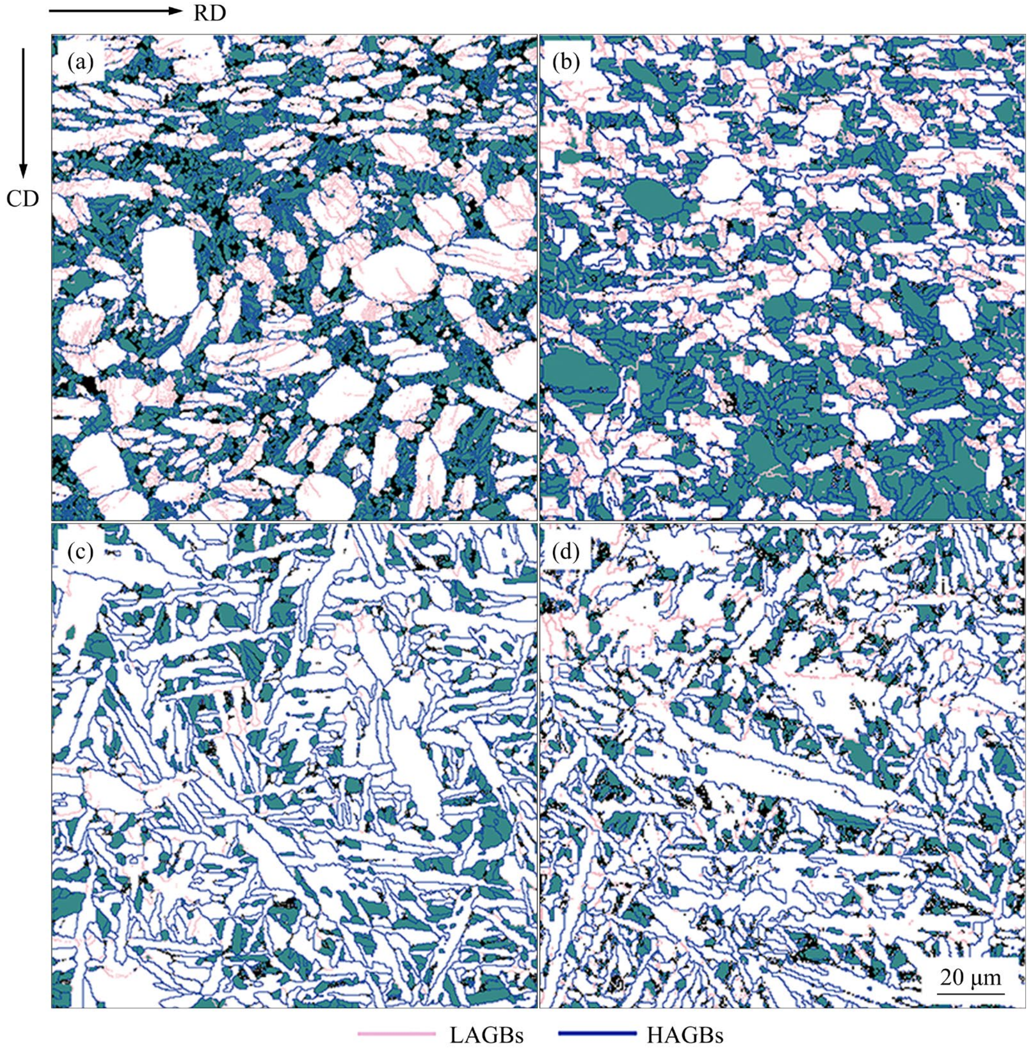

Fig. 8 Recrystallized fraction maps of Ti−6Al−4V−0.5Mo−0.5Zr alloy samples deformed at different temperatures and strain rate of 10 s^{-1} (Green covered area meaning DRX part (GOS value <1.6°), white covered area meaning deformed part (GOS value >1.6°)): (a) T=890 °C, $\dot{\varepsilon}$=10 s^{-1}; (b) T=930 °C, $\dot{\varepsilon}$=10 s^{-1}; (c) T=970 °C, $\dot{\varepsilon}$=10 s^{-1}; (d) T=1030 °C, $\dot{\varepsilon}$=10 s^{-1}

The misorientation angle distribution charts are also illustrated in Fig. 7. At deformation temperatures of 890 and 930 °C, the proportions of LAGBs were 31.71% and 19.62%, respectively. Moreover, a quantity of initially deformed α grains with substructure emerged significantly. At deformation temperatures of 930, 990, and 1030 °C, the peaks in the orientation distribution angles appeared at specific positions (55°−65° and 85°−90°). These peaks corresponded to the HAGBs between the α variants formed through the transformation of the same or different β phase grains [35−38]. The α variants represent the α phase cluster that formed via the $\beta\rightarrow\alpha$ transformation within the original β grain.

The microstructure evolution during hot deformation process was elucidated based on EBSD observation. In particular, variations in the internal orientation angle distributions were employed to differentiate between recrystallized and deformed grain within the alloy. The grain orientation spread (GOS) that refers to the average difference between the average crystal orientation and all the measured grain orientation, can be expressed as [39]

$$\mathrm{GOS}=\frac{1}{N}\sum_{A=1}^{N}\left\{\min\left[\cos^{-1}\left(\frac{\mathrm{trace}\left[g_{\mathrm{ave}}h_i g^{A^{-1}}\right]-1}{2}\right)\right]\right\} \quad (2)$$

where N is the number of measured points in a certain grain, A represents one measured point, g_{ave}

is the average orientation of grain, g^A is the orientation measured at Position A, and h_i is the minimum misorientation angle between average orientation and measurement Point A. It can be obtained that the GOS parameters are essentially independent of step size as long as several measurements are performed within the grain, making it an ideal measurement method for determining the proportion of recrystallized structure. The GOS approach is based on the principle that the grain orientation spread of the DRX grain is lower than that of the deformed grain. DRX grains, with their reduced dislocation density, typically result in low GOS values. Combined with the GOS statistics function in the EBSD data analysis software, a GOS threshold of 1.6° was determined to distinguish DRX grains from deformed grains.

The DRX region can be delineated according to the GOS threshold obtained from Eq. (2) combined with the EBSD analysis software, as shown in Fig. 8. Fine DRX α grains were observed under different deformation conditions. The deformed microstructure in $\alpha+\beta$ phase region exhibited DRX volume fractions of 32.72% (T=890 °C, $\dot{\varepsilon}=10\ \mathrm{s}^{-1}$) and 45.40% ($T$=930 °C, $\dot{\varepsilon}=10\ \mathrm{s}^{-1}$), as depicted in Figs. 8(a) and (b), respectively. In conjunction with the rheological curve, this indicates that under these conditions, the DRX of the initial phase is the predominant mechanism of dynamic softening. By comparison, in the β phase region, the volume fractions of the secondary α clusters that underwent DRX were 17.21% (T=970 °C, $\dot{\varepsilon}=10\ \mathrm{s}^{-1}$) and 13.44% ($T$=1030 °C, $\dot{\varepsilon}=10\ \mathrm{s}^{-1}$), as shown in Figs. 8(c) and (d), respectively. In this case, the DRX of the secondary α clusters was not predominant. Finally, as shown in Fig. 4, the original β phase also underwent DRX at high temperatures.

Continuous dynamic recrystallization (CDRX) usually occurs in alloys with high stack fault energy, and it is typically accompanied by DRV and the transition from LAGs to HAGs [40]. Furthermore, CDRX occurs through the gradual rotation of subgrain adjacent to pre-existing grain boundary, which produces a significant gradient in the boundary orientations from the center to the edge of the previous grain. Therefore, it is possible to determine whether the cumulative orientation angle is greater than 15° [41,42]. Figure 9 shows the EBSD map at a deformation temperature of 890 °C and strain rate of 10 s^{-1}. In this context, "point-to-point" misorientation indicates local misorientation differences, whereas "point-to-origin" misorientation represents the cumulative misorientation measured from a fixed reference point.

Referring to Fig. 9(a), the large deformed grain was divided into subgrain by subgrain boundary. Moreover, as referenced in Fig. 9(b), the cumulative orientation angle from the center Point A to the edge Point B of the large grain was 17°, indicating that the progressive subgrain process inside the grain was more active. The "point-to-point" misorientation, observed at distance of 1.56 and 7.35 μm from Point A, shows a peak misorientation of 6°. This suggests that the orientation distribution difference changed abruptly at the subgrain boundary, while it remained relatively stable within the grain themselves. The accumulated dislocation

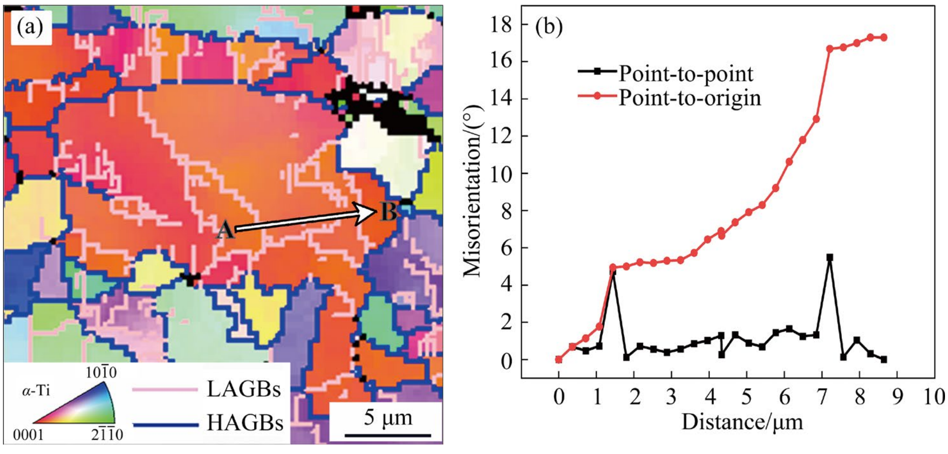

Fig. 9 DRX mechanism of Ti−6Al−4V−0.5Mo−0.5Zr alloy (T=890 °C, $\dot{\varepsilon}=10\ \mathrm{s}^{-1}$): (a) EBSD map; (b) Misorientation distribution from Point A to Point B

at subgrain boundary underwent a transition from LAGs to HAGs, which is typical CDRX [43]. This phenomenon became more pronounced during the deformation in $\alpha+\beta$ phase region.

4 Conclusions

(1) The stress began to display more noticeable oscillation with an increase of strain rate. In $\alpha+\beta$ phase region, the flow stress initially increased with increasing strain until it reached a peak, beyond which it decreased until a steady state, this was related to the DRX. In β phase region, the flow stress reached a peak and then gradually stabilized as the strain increased. This was attributed to the combined effects of work hardening and DRV.

(2) In $\alpha+\beta$ phase region, the $\alpha\to\beta$ transformation was incomplete. As the deformation temperature increased, the extent of transformation to β phase also increased, resulting in a gradual reduction in the initial proportion of α grain. In β phase region, DRV was the primary thermal deformation mechanism. The fragment degree of stripe α phase increased with the strain rate at 910 °C.

(3) In $\alpha+\beta$ phase region, distinct CDRX of α grain and lamellar fragment occurred during deformation. In β phase region, DRX of β grain occurred, and the lamellar α phase initially precipitated within β grain, which subsequently underwent DRX. The volume fraction of the secondary α cluster where DRX occurred at temperature up to 1030 °C was less than 20%. Therefore, the DRX of secondary α cluster was not dominant.

CRediT authorship contribution statement

Zhen-ni ZHOU: Methodology, Investigation, Formal analysis, Writing − Original Draft, Writing − Review & editing; **Gao-yong LIN:** Conceptualization, Methodology, Writing − Review & editing, Resources; **Yu-hao AI:** Conceptualization, Methodology, Writing − Review & editing, Resources; **Wei-zhong FENG:** Writing − Review & editing; **Ping-hui ZHANG:** Formal analysis, Visualization; **Hui-qun LIU:** Funding acquisition, Data curation.

Declaration of competing interest

The authors declare that they have no known competing financial interests or personal relationships that could have appeared to influence the work reported in this paper.

Acknowledgments

This research was funded by the National Key Research and Development Program of China (No. 2021YFB3700803), and the State Key Laboratory of Powder Metallurgy, Central South University, Changsha, China.

References

[1] MAHLOBO M G R, CHIKOSHA L, OLUBAMBI P A. Study of the corrosion properties of powder rolled Ti−6Al−4V alloy applied in the biomedical implants [J]. Journal of Materials Research and Technology, 2022, 18: 3631−3639. DOI: 10.1016/j.jmrt.2022.04.004

[2] SURESH S, SUN C N, TEKUMALLA S, ROSA V, LING NAI S M, WONG R C W. Mechanical properties and in vitro cytocompatibility of dense and porous Ti−6Al−4V ELI manufactured by selective laser melting technology for biomedical applications [J]. Journal of the Mechanical Behavior of Biomedical Materials, 2021, 123: 104712. DOI: 10.1016/j.jmbbm.2021.104712

[3] LIU Qiang, TONG Ke, ZHU Guo-chuan, TAN Yi, ZHANG Juan-tao, XU Xin, LI Xiao-jun, SONG Sheng-yin. Investigation of fracture causes of the titanium alloy drill pipe in ultra-short radius horizontal well drilling [J]. Engineering Failure Analysis, 2022, 140: 106516. DOI: 10.1016/j.engfailanal.2022.106516

[4] LIU Tian-yu, MIN Xiao-hua, ZHANG Shuang, WANG Cun-shan, DONG Chuang. Microstructures and mechanical properties of Ti−Al−V−Nb alloys with cluster formula manufactured by laser additive manufacturing [J]. Transactions of Nonferrous Metals Society of China, 2021, 31: 3012−3023. DOI: 10.1016/S1003-6326(21)65711-4

[5] TANG Huan-chun, ZHAO Da-peng, WAN Chang-jun, LI Xiao-song, JI Xiao-wei, TANG Jin-cheng, CAO Yuan-kui, LIU Yong. Influence of heterogeneous microstructures on anodization behavior and biocompatibility of Ti−15Zr alloy [J]. Transactions of Nonferrous Metals Society of China, 2023, 33: 2076−2089. DOI: 10.1016/S1003-6326(23)66245-4

[6] LIN Hao-qin, LING Jin-feng, CHEN Wei-min, WANG Yao, WU Xiao-ke, ZHANG Li-jun. High-throughput determination of mechanical and diffusion properties of Ti−Ta−Fe alloys [J]. Transactions of Nonferrous Metals Society of China, 2022, 32: 3963−3972.

[7] YANG Jun-zhou, WU Jian-jun, XIE Hai-nan, LI Zhi-guo, WANG Kai-wei. Mechanism of continuous dynamic recrystallization of Ti−6Al−4V alloy during superplastic forming with sub-grain rotation [J]. Transactions of Nonferrous Metals Society of China, 2023, 33: 777−788. DOI: 10.1016/j.matchar.2018.09.004

[8] LU Tong, DAN Zhen-hua, LI Kai, YI Dan-qing, ZHOU Lian, CHANG Hui. Hot deformation behaviors and dynamic recrystallization mechanism of Ti-35421 alloy in β single field [J]. Transactions of Nonferrous Metals Society of China,

2022, 32: 2889−2907. DOI: 10.1016/S1003-6326(22)65991-0

[9] CHEN Dong, YANG Qian-ru, YANG Na-chuan, WANG Meng, XU Qiang, WU Jing-yuan, JIANG Yan-bin, LI Zhou, XIAO Zhu, WEI Hai-gen. Hot compressive deformation and microstructural evolution of 60NiTi alloy [J]. Transactions of Nonferrous Metals Society of China, 2023, 33: 189−200. DOI: 10.1016/S1003-6326(22)66099-0

[10] LIU Shi-feng, SHI Jia-min, YANG Xiao-kang, CAI Jun, WANG Qing-juan. High-temperature flow behaviour and constitutive equations for a TC17 titanium alloy [J]. High Temperature Materials and Processes, 2019, 38: 168−177. DOI: 10.1515/htmp-2017-0145

[11] HUANG Xiao-min, ZANG Yong, GUAN Ben. Constitutive models and microstructure evolution of Ti−6Al−4V alloy during the hot compressive process [J]. Materials Research Express, 2021, 8: 016534. DOI: 10.1088/2053-1591/abdaf0

[12] YESHANEW S K, BAI Chun-guang, JIA Qing, XI Tong, ZHANG Zhi-qiang, LI Diao-feng, XIA Zhi-zhou, YANG Rui, YANG Ke. Influence of hot-rolling deformation on microstructure, crystalline orientation, and texture evolution of the Ti6Al4V5Cu alloy [J]. Acta Metallurgica Sinica (English Letters), 2023, 36: 1261−1280. DOI: 10.1007/s40195-023-01544-5

[13] LIU Chang, ZHANG Jiian-bo, YANG Yii-kai, XIA Xing-chuan, HE Tian, DING Jian, TANG Ying, ZHANG Zan, CHEN Xue-guang, LIU Yong-chang. Hot deformation behavior of ATI 718Plus alloy with different microstructures [J]. Acta Metallurgica Sinica (English Letters), 2022, 35: 1383−1396. DOI: 10.1007/s40195-021-01361-8

[14] XIA Yu-feng, JIANG Wei, CHENG Qian, JIANG Lai, JIN Li. Hot deformation behavior of Ti−6Al−4V−0.1Ru alloy during isothermal compression [J]. Transactions of Nonferrous Metals Society of China, 2020, 30: 134−146. DOI: 10.1016/S1003-6326(19)65186-1

[15] KHERROUBA N, BOUABDALLAH M, BADJI R, CARRON D, AMIR M. Beta to alpha transformation kinetics and microstructure of Ti−6Al−4V alloy during continuous cooling [J]. Materials Chemistry and Physics, 2016, 181: 462−469. DOI: 10.1016/j.matchemphys.2016.06.082

[16] LI Kai, YANG Ping. Strain-induced α-to-β phase transformation during hot compression in Ti−5Al−5Mo−5V−1Cr−1Fe alloy [J]. Transactions of Nonferrous Metals Society of China, 2019, 29: 296−304. DOI: 10.1016/S1003-6326(19)64939-3

[17] HUANG Liang, LI Chang-min, LI Chen-lin, HUI Song-xiao, YU Yang, ZHAO Ming-jie, GUO Shi-qi, LI Jian-jun. Research progress on microstructure evolution and hot processing maps of high strength β titanium alloys during hot deformation [J]. Transactions of Nonferrous Metals Society of China, 2022, 32: 3835−3859. DOI: 10.1016/S1003-6326(22)66062-X.

[18] GANGIREDDY S. Effect of initial microstructure on high-temperature dynamic deformation of Ti−6Al−4V alloy [J]. Metallurgical and Materials Transactions A, 2018, 49: 4581−4594. DOI: 10.1007/s11661-018-4774-1

[19] AO Ni, LIU Dao-xin, LIU Cheng-song, ZHANG Xiao-hua, LIU Dan. Face-centered titanium induced by ultrasonic surface rolling process in Ti−6Al−4V alloy and its tensile behavior [J]. Materials Characterization, 2018, 145: 527−533. DOI: 10.1016/j.matchar.2018.09.004

[20] ZHU Y C, ZENG W D, LIU J L, ZHAO Y Q, ZHOU Y G, YU H Q. Effect of processing parameters on the hot deformation behavior of as-cast TC21 titanium alloy [J]. Materials & Design, 2012, 33: 264−272. DOI: 10.1016/j.matdes.2011.07.018

[21] CHEN Xue-wen, ZHANG Bo, DU Yu-qing, LIU Meng-xiang, BAI Rong-ren, SI Ya-hui, LIU Bing-qi, JUNG Dong-won, OSAKA A. Constitutive model parameter identification based on optimization method and formability analysis for Ti6Al4V alloy [J]. Materials, 2022, 15: 1748. DOI: 10.3390/ma15051748

[22] FAN J K, KOU H C, LAI M J, TANG B, CHANG H, LI J S. Characterization of hot deformation behavior of a new near beta titanium alloy: Ti-7333 [J]. Materials & Design, 2013, 49: 945−952. DOI: 10.1016/j.matdes.2013.02.044

[23] MITCHELL T E, HIRTH J P, MISRA A. Apparent activation energy and stress exponent in materials with a high Peierls stress [J]. Acta Materialia, 2002, 50: 1087−1093. DOI: 10.1016/S1359-6454(01)00409-8

[24] KIM Y M, SONG Y B, LEE S H, KWON Y S. Characterization of the hot deformation behavior and microstructural evolution of Ti−6Al−4V sintered preforms using materials modeling techniques [J]. Journal of Alloys and Compounds, 2016, 676: 15−25. DOI: 10.1016/j.jallcom.2016.03.146

[25] TONG Yue, LIN Gao-yong, WU Yu, PAN Qian-fu, ZHUO Hong, LIU Hun-qun. Constitutive equation for the hot deformation and microstructure evolution of 12Cr-F/M steel [J]. Steel Research International, 2023, 94: 2200660. DOI: 10.1002/srin.202200660

[26] SESHACHARYULU T, MEDEIROS S C, FRAZIER W G, PRASAD Y V R K. Hot working of commercial Ti−6Al−4V with an equiaxed α−β microstructure: materials modeling considerations [J]. Materials Science and Engineering A, 2000, 284: 184−194. DOI: 10.1016/S0921-5093(00)00741-3

[27] LIU Jiang-lin, ZENG Wei-dong, LAI Yun-jin, JIA Zhi-qiang. Constitutive model of Ti17 titanium alloy with lamellar-type initial microstructure during hot deformation based on orthogonal analysis [J]. Materials Science and Engineering A, 2014, 597: 387−394. DOI: 10.1016/j.msea.2013.12.076.

[28] CHEN Zhao-qi, XU Li-juan, CAO Shou-zhen, YANG Jin-kai, ZHENG Yun-fei, XIAO Shu-long, TIAN Jing, CHEN Yu-yong. Characterization of hot deformation and microstructure evolution of a new metastable β titanium alloy [J]. Transactions of Nonferrous Metals Society of China, 2022, 32: 1513−1529. DOI: 10.1016/S1003-6326(22)65890-4

[29] YU Xiao-yu, XIAO Zhou, LI Zhou, ZHAO Xin-si, LU Si-jian, FU Yuan-yuan. Hot deformation behaviour and microstructure evolution of gold-imitation brass alloy with high corrosion resistance [J]. Transactions of Nonferrous Metals Society of China, 2023, 33: 839−850. DOI: 10.1016/S1003-6326(23)66150-3.

[30] JI Zhe, SHEN Cheng-jin, WEI Fu-xiang, LI Hong-wei. Dependence of macro- and micro-properties on α plates in Ti−6Al−2Zr−1Mo−1V alloy with tri-modal microstructure [J]. Metals, 2018, 8: 299. DOI: 10.3390/met8050299

[31] LIN Y C, HUANG Jian, LI Hong-bin, CHEN Dong-dong. Phase transformation and constitutive models of a hot compressed TC18 titanium alloy in the $\alpha+\beta$ regime [J].

Vacuum, 2018, 157: 83−91. DOI: 10.1016/j.vacuum.2018.08.020

[32] SHEHATA M M, EL-HADAD S, SHERIF M, IBRAHIM K M, FARAHAT A I Z, ATTIA H. Influence of microstructure and alloy composition on the machinability of *α*/*β* titanium alloys [J]. Materials, 2023, 16: 688. DOI: 10.3390/ma16020688

[33] MAHADULE D, KUMAR D, DANDEKAR T R, KHATIRKAR R K, SUWAS S. Modelling of flow stresses during hot deformation of Ti−6Al−4Mo−1V−0.1Si alloy [J]. Journal of Materials Research, 2023, 38(15): 3750−3763. DOI: 10.1557/s43578-023-01097-4

[34] WANG Min, ZHOU Jian-xin, YIN Ya-jun, NAN Hai, XUE Peng-ju, TU Zhi-xin. Hot deformation behavior of the Ti6Al4V alloy prepared by powder hot isostatic pressing [J]. Journal of Alloys and Compounds, 2017, 721: 320−332. DOI: 10.1016/j.jallcom.2017.06.003

[35] ROY S, SUWAS S. The influence of temperature and strain rate on the deformation response and microstructural evolution during hot compression of a titanium alloy Ti−6Al−4V−0.1B [J]. Journal of Alloys and Compounds, 2013, 548: 110−125. DOI: 10.1016/j.jallcom.2012.08.123

[36] GEY N, HUMBERT M. Characterization of the variant selection occurring during the *α*→*β*→*α* phase transformations of a cold rolled titanium sheet [J/OL]. Acta Materialia, 2002, 50: 277−287. DOI: 10.1016/S1359- 6454(01)00351-2

[37] MACLEOD S G, ERRANDONEA D, COX G A, CYNN H, DAISENBERGER D, FINNEGAN S E, MCMAHON M I, MUNRO K A, POPESCU C, STORM C V. The phase diagram of Ti−6Al−4V at high-pressures and high-temperatures [J]. Journal of Physics: Condensed Matter, 2021, 33: 154001. DOI: 10.1088/1361-648X/abdffa

[38] YU Yong-zheng, SHI Ru-yu, ZHANG Yang, LIU Li-yuan, LI Jun-peng, GUO Chun-huan, JIANG Feng-chun, LIAW P K, ZHANG Zhong-wu. Nanoprecipitate improves high strainrate deformability in a high-entropy alloy [J]. Tungsten, 2024. DOI: 10.1007/s42864-024-00295-9.

[39] DONG Shu-lin, CHEN Rui-run, GUO Jing-jie, DING Hong-sheng, SU Yan-qing, FU Heng-zhi. Deformation behavior and microstructural evolution of directionally solidified TiAlNb-based alloy during thermo-compression at 1373−1573 K [J]. Materials & Design, 2015, 84: 118−132. DOI: 10.1016/j.matdes.2015.06.117

[40] CHEN Rui-run, MA Teng-fei, GUO Jing-jie, DING Hong-sheng, SU Yan-qing, FU Heng-zhi. Deformation behavior and microstructural evolution of hydrogenated Ti44Al6Nb alloy during thermo-compression at 1373−1523 K [J]. Materials & Design, 2016, 108: 259−268. DOI: 10.1016/j.matdes.2016.06.083

[41] LI Chang-min, HUANG Liang, ZHAO Ming-jie, GUO Shi-qi, LI Jian-jun. Hot deformation behavior and mechanism of a new metastable *β* titanium alloy Ti−6Cr−5Mo−5V−4Al in single phase region [J]. Materials Science and Engineering A, 2021, 814: 141231. DOI: 10.1016/j.msea.2021.141231

[42] WU Zao-ming, HE Lin, YE Lin-sen, YANG Xiao-feng, Hong Bo. High-dense nanocrystalline W-based alloy prepared by hot isostatic pressing with uniform micro-structure, ultrahigh hardness and good thermal stability [J]. Tungsten, 2025, 7(1): 120−136. DOI: 10.1007/s42864-024-00296-8.

[43] SUN Yong-gang, ZHANG Chang-jiang, FENG Hong, ZHANG Shu-zhi, HAN Jian-chao, ZHANG Wang-gang, ZHAO Er-tuan, WANG Hong-wei. Dynamic recrystallization mechanism and improved mechanical properties of a near *α* high temperature titanium alloy processed by severe plastic deformation [J]. Materials Characterization, 2020, 163: 110281. DOI: 10.1016/j.matchar.2020.110281.

石油钻用 Ti−6Al−4V−0.5Mo−0.5Zr 钛合金的热变形特征及动态再结晶行为

周珍妮[1]，林高用[1]，艾宇浩[1]，凤伟中[2]，张平辉[2]，刘会群[1]

1. 中南大学 材料科学与工程学院，长沙 410083；

2. 宝鸡钛业股份有限公司，宝鸡 721014

摘　要：研究在变形温度为 890~1030 ℃和应变速率为 0.01~10 s^{-1} 条件下 Ti−6Al−4V−0.5Mo−0.5Zr 钛合金的高温变形行为，同时分析相应的动态再结晶(DRX)机理。研究结果表明，在不同的变形条件下会出现不同程度的应力振荡现象。在 $\alpha+\beta$ 两相区高温变形过程中，应力−应变曲线表现出明显的 DRX 特征。当变形温度低于 950 ℃时，出现明显的 α 晶粒连续动态再结晶和条状相的断裂现象。当变形温度高于 950 ℃时，β 相和部分次生 α 相集束发生 DRX。

关键词：钛合金；应力−应变曲线；应力振荡；动态再结晶

(Edited by Xiang-qun LI)